Investigation on the effect of coulomb friction on nose landing gear shimmy

Mohsen Rahmani and Kamran Behdinan

Version Post-print/accepted manuscript

Citation (published version) Rahmani, M., & Behdinan, K. (2018). Investigation on the effect of coulomb friction on nose landing gear shimmy. Journal of Vibration and Control, 1077546318774440.

Corresponding Author:

Mohsen Rahmani, Department of Mechanical and Industrial Engineering, University of Toronto, 5 King's College Road, Toronto, Ontario, Canada, M5S 3G8

Email: mohsen.rahmani@mail.utoronto.ca

Investigation on the effect of coulomb friction on nose landing gear shimmy

Mohsen Rahmani[1]. Kamran Behdinan[2]

[1]Graduate Student, Advanced Research Lab for Multifunctional Lightweight Structures (ARL-MLS), Department of Mechanical and Industrial Engineering, University of Toronto, Canada

[2]Professor of Mechanical Engineering, Advanced Research Lab for Multifunctional Lightweight Structures (ARL-MLS), Department of Mechanical and Industrial Engineering, University of Toronto, Canada

Abstract

Landing gear shimmy remains a challenge in aircraft design despite abundant advances in aircraft engineering in the past few decades. Accurate shimmy prediction is closely tied to availability of dynamic models with all relevant types of motions and key nonlinear elements, a matter which has been accomplished in the present study through including rotational, lateral, longitudinal, and axial degrees of freedom and tire, shock absorber, and Coulomb friction nonlinearities. Using Multi-Body Dynamic simulations, stability of the nose landing gear is studied as a function of key system parameters. Influences of nonlinearities are investigated in isolation, with a more in-depth look at the Coulomb friction effect, which is modeled as a function of the shock absorber stroke rate and rotational shimmy speed. It is found that Coulomb friction is a key factor in determining the onset and type of shimmy. The effect of friction parameters is then studied using nonlinear sensitivity analyses, and witnessed trends are utilized to draw design recommendations.

Keywords

Nonlinear vibration, landing gear, shimmy, Coulomb friction, Stability Analysis

1. Background

Landing gear (LG) shimmy is described as self-induced torsional and lateral oscillations typically in the range of 10-30Hz, arising from the coupling of LG structure, elastic tire(s), and the fuselage structure during the aircraft ground operations. Shimmy can result in impairing the pilot's visibility and control, passenger discomfort, gear structural damage, and sudden failure of the gear (Krüger et al., 1997). This phenomenon can occur on both nose landing gear (NLG) and main landing gear (MLG) during landing, take-off,

and taxying, yet it is more common in NLG. It is understood that shimmy mode is excited due to transfer of kinetic energy from the moving aircraft to the wheels (Arreaza et al., 2016), acting as the energy source for the undesired oscillations. Close to 60% of aircraft failures are related to LG systems with fatigue due to multi-axial loads (e.g. shimmy loads) being the number one cause (Lok et al., 2014). Accidents due to shimmy are reported in the literature (Van Der Valk et al., 1993; CIAIAC, 1999; Eret et al., 2015) whose root cause is commonly laying in inadequate design. It is crucial to prevent reoccurrence of such events through appropriate design decisions. Accurate shimmy prediction and its effective suppression is then imperative to ease aviation risk and cost.

1.1. Shimmy Modeling and Solution Approaches

LG is intrinsically a nonlinear system. Linearization of the equations (Arreaza et al., 2016) or calculating equivalent properties from energy methods (Grossman, 1980) enables us to employ well-established linear analysis techniques. In terms of model degrees of freedom (DoF), while some form of rotational and lateral motion is captured in the majority of shimmy models, few of them include longitudinal and axial motions as well. Tire-ground interaction is mainly represented by Stretched String tire model (Von Schlippe and Dietrich, 1947) and sometimes by alternative approaches such as Moreland's model (Moreland, 1954), Magic Formula (Pacejka, 2009), and Rigid Ring tire model (Zegelaar and Pacejka, 1996). Due to nonlinearity and complexity of the LG system, closed-form solutions are not pursued and one needs to resort to numerical solutions. Numerical integration of nonlinear equations is effective in predicting stable and unstable limit-cycles, as well as transient and steady-state response of the system. Numerical continuation method, often referred to as Bifurcation Analysis, is employed as well (Howcroft et al., 2013; Kewley et al., 2016; Thota et al., 2008, 2010) in which one or more of parameters are altered continuously and system stability characteristics are inferred from 2D and 3D plots in the parameter space.

Analytical models are prevalent in the literature (Esmailzadeh et al., 1999; Howcroft et al., 2013; Kewley et al., 2016; Sura et al., 2007; Thota et al., 2008) which are frequently handled using numerical continuation or time integration. Multi-Body Dynamic (MBD) simulation (Gualdi et al., 2008; Khapane, 2003, 2006; Krason et al., 2015; Krüger et al., 2011) is another versatile tactic to obtain the time response of dynamic systems. The MBD model is assembled in a modular manner and it can be modified without the necessity to manually update equations of motion. Other methods also employed in shimmy studies include Quasi-linear analysis (Krüger and Morandini, 2011), Describing Functions (Burton, 1981), Multiple Time Scales (Gordon, 2002), and Harmonic Balance (Padmanabhan et al., 2015; Zhou et al., 2005).

A classification of shimmy models based on state-space formulation order is beneficial to understand the contribution of the present work. A third-order LG model by Somieski (1997) and a similar one in a study by Airbus (Coetzee, 2007) include the rotational DoF and lateral deflection of the tire patch. A study by Boeing (Gordon, 2002) employs a similar model but adds rotational freeplay and a fixed Coulomb torque. Atabay and Ozkol (2013) reused Somieski's model and incorporated a magnetorheological damper for shimmy suppression. A fifth-order model by Thota et al. (2008) including rotational and lateral DoFs incorporates rake angle and effective caster length. Feng et al. (2015) added

freeplay with linear and velocity-squared damping to the fifth-order model and found freeplay to be destabilizing the system. The model by Sura and Suryanarayan (2007) employing Moreland's tire model and the one by Liu et al. (2015) are also fifth-order. A dual-wheel NLG model was used by Eret et al. (2015) to study the effect of noise reduction apparatus on stability of the gear. Addition of longitudinal DoF of the gear led to the seventh-order NLG model (Thota et al., 2010). Howcroft et al. (2015) presented a tenth-order model of the MLG which features two independent wheels, as well as the axial DoF.

1.2. Dealing with Nonlinearities

Friction, freeplay, Oleo-pneumatic shock absorber, and the tire dynamics are primary sources of nonlinearity in the NLG system. Coulomb friction and Oleo-pneumatic shock absorber are frequently disregarded while rotational freeplay has been relatively addressed in the literature. Freeplay can have a major influence on LG stability, ranging from a shift in the critical shimmy speed to introduction of bi-stable and more complex shimmy modes (Howcroft et al., 2013; Sura et al., 2007). Tire nonlinearity is ignored whenever a linear tire model is assumed. Nonlinear Oleo-pneumatic shock absorber has been implemented in a few works (Gualdi et al., 2008; Khapane, 2003) although its definite effect on shimmy is not examined. Substantial friction develops in the Oleo-pneumatic shock absorber in slip and stick modes (Krüger et al., 1997). Since friction dissipates energy it has a stabilizing effect and alleviates the subcritical limit-cycles of the nonlinear system (Arreaza et al., 2016; Padmanabhan and Dowell, 2015) as observed in physical tests as well (Pritchard, 2001). Coulomb friction is typically modeled as a constant torque, while an effective damping coefficient representing Coulomb friction (Padmanabhan and Dowell, 2015) and hysteresis characteristic for Coulomb friction (Somieski, 2001) have also been proposed.
Although sources of nonlinearity have been studied to different extents, studies with all key nonlinearities and DoFs, along with an investigation of their effects on shimmy appears to be lacking from the literature. Especially, to the best of our knowledge, the effect of Coulomb friction has only been tackled using simple LG models and without its dependency on the nonlinear shock absorber. Therefore, the emphasis of this work is on the detailed nonlinear NLG modeling, along with investigating the friction effect based on an innovative Coulomb model.

2. Fundamentals

2.1. Landing Gear Model: Overall

The bulk of shimmy studies account for the rotational-lateral dynamics only, assuming longitudinal DoF would only weakly couples with it (Van Der Valk et al., 1993; Eret et al., 2015; Thota et al., 2010), while the possibility of coupling has been confirmed in more recent works (Howcroft et al., 2013). Furthermore, the change in gear length due to the shock absorber compression affects the dynamics and structural characteristics (e.g. moment of inertia). Hence, inclusion of all four DoFs is imperative for accurate shimmy response prediction.

The inputs of the NLG model are vertical force from the airframe F_z and forward velocity of the aircraft V. The outputs sought are rotational and lateral vibrations which comprise limit-cycles of this nonlinear system. As shown in the schematic of the dynamic model in Figure 1, P_T is the airframe attachment point while the motion of the bottom of the gear P_B is of primary interest here. The four structural DoFs designated in Figure 1 are:
Rotational (ψ): designates total rotation about the strut axis, of P_B relative to P_T.
Lateral (δ): designates total rotation about the roll axis X, of P_B relative to P_T.
Longitudinal (β): designates total rotation about the pitch axis Y, of P_B relative to P_T.
Axial (η): designates total shock absorber piston displacement along the strut axis.

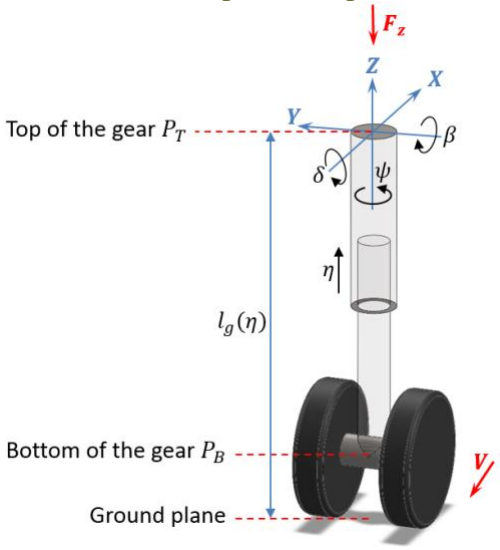

Figure 1. Schematic of the NLG dynamic model with relevant DoFs and inputs

The governing equations of the proposed NLG model are of the following form:

$$I_z\ddot{\psi} + k_\psi\psi + c_\psi\dot{\psi} + M_{T_\psi} + M_{Z_\psi} + T_{CLM} = 0 \quad (1)$$

$$I_x\ddot{\delta} + k_\delta\delta + c_\delta\dot{\delta} + M_{T_\delta} + M_{Z_\delta} = 0 \quad (2)$$

$$I_y\ddot{\beta} + k_\beta\beta + c_\beta\dot{\beta} + M_{T_\beta} + M_{Z_\beta} = 0 \quad (3)$$

in which M_{T_ψ} is the moment term applied by the tire (T) to the rotational (ψ) DoF which includes contributions of the tire's self-aligning moment and restoring force, as well as the tire's tread damping, all of which are explained in the Tire Dynamics section. Tire moments have components applied to lateral and longitudinal motions as well, denoted by M_{T_δ} and M_{T_β} respectively. The vertical force (F_z) generates moments along all three directions as well, designated by M_{Z_ψ}, M_{Z_δ}, M_{Z_β} in the equations. The Coulomb friction torque T_{CLM} is applicable only to the rotational motion. The strokes representing lateral and longitudinal motions are given by $\delta^* = \delta l_g$ and $\beta^* = \beta l_g$.

2.2. Tire Dynamics

Nonlinear tire dynamic is accounted for based on Stretched String theory (Von Schlippe and Dietrich, 1947) which represents the tire as a massless elastic string in contact with the ground along a finite length of h referred to as contact patch, as shown in Figure 2. It

assumes that the force and moment developed at the tire-ground interface are a function of the characteristic deflection of the tire patch. Moreover, an exponentially decaying deflection in a region designated as the relaxation length L is envisioned (Gordon, 2002; Somieski, 1997). Here, the theory is presented based on the formulation of Thota et al. (2010) who added to the original formulation the effect of lateral and longitudinal motions, as well as the influence of the rake angle ϕ on the leading point deformation λ. The characteristic tire equation then reads:

$$\dot{\lambda} + \frac{V}{L}\lambda - V\,sin(\psi\,cos(\phi+\beta)) - l_g\dot{\delta}\,cos(\delta) - \left(e_{eff} - h\right)cos(\psi\,cos(\phi+\beta))\,\dot{\psi}\,cos(\phi+\beta) = 0 \quad (4)$$

As shown in Figure 2, the lateral deformation of the leading point is linked to the slip angle α through $\alpha = \tan^{-1}\lambda/L$. The effective caster length e_{eff} is the distance from the center of contact patch to the intersecting point of strut centerline and the ground plane ($e = e_{eff}$ in the case of $\phi = 0$ and $\beta = 0$). A self-aligning moment $M_{k\alpha}$ and a restoring force $F_{k\lambda}$ are generated at the interface due to the tire deformation. These terms can be approximated using the following relationships (Thota et al., 2010):

$$M_{K_\alpha}/F_z = \begin{cases} k_\alpha(\alpha_m/\pi)\,sin(\alpha\pi/\alpha_m) & if\ |\alpha| \le \alpha_m \\ 0 & if\ |\alpha| > \alpha_m \end{cases} \quad (5)$$

$$F_{K_\lambda}/F_z = k_\lambda\,tan^{-1}(7\,tan(\alpha))\,cos(0.95\,tan^{-1}(7\,tan(\alpha))) \quad (6)$$

In the above, k_α and k_λ are self-aligning moment and restoration force coefficients and α_m is the slip angle limit. Additionally, a moment term due to tire's tread damping is also created (Thota et al., 2010) which is described as:

$$M_{D_\lambda} = c_\lambda\dot{\psi}/V \quad (7)$$

in which c_λ is the tire damping coefficient. Both M_{K_α} and M_{D_λ} moments are assumed to be perpendicular to the ground plane.

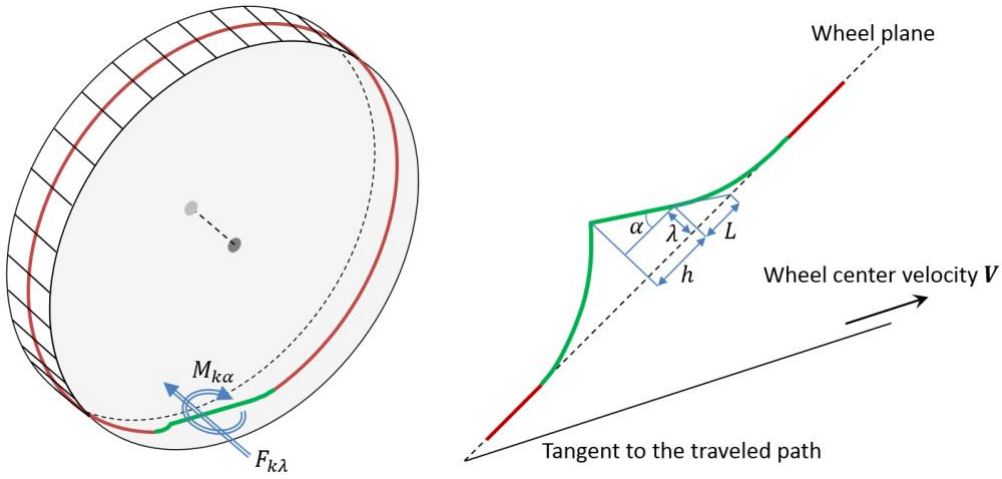

Figure 2. Stretched String representation of the tire (left), and top view of the tire-ground contact area (right)

In the proposed MBD model, the instantaneous tire force and moments are applied at the physical location of the tire patch midpoint, leading to precise moments applied to the structure in all directions, while nearly all of the existing analytical models simply consider the component of the moment about the strut axis. The tire vertical deflection d_t

is accounted for too, as it affects moment arms through altering the gear length according to:

$$l_g = l_{g_0} - \eta - d_t \cos(\phi + \beta) \tag{8}$$

where l_{g_0} is the gear length in neutral state ($F_z = 0$), measured along the strut axis from fuselage attachment to the ground plane. This dependency is normally neglected due to assuming a fixed-length gear. Here the tire model is augmented by incorporating the vertical stiffness using available representative force-deflection data shown in Figure 3.

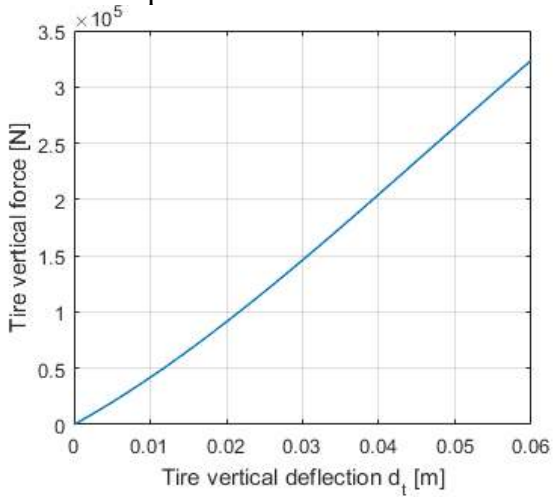

Figure 3. Tire vertical force-deflection curve obtained from NASA report (Daniels, 1996) and scaled 5X to reflect the greater range of airframe forces being considered in this work

2.3. Oleo-pneumatic Shock Absorber

As suggested by Khapane (2003), the gas spring of the Oleo-pneumatic shock absorber can be described by the polytropic expansion law as:

$$F_s = F_0 \left[1 - \left(\frac{\eta}{\eta_m}\right)\right]^{-nc_k} \tag{9}$$

In the above F_s, F_0, η, η_m, n, and c_k are spring force, pre-stress force, spring stroke, maximum stroke, polytropic coefficient and its correction factor respectively. The damping force from oil flow through orifices is specified as:

$$F_d = d\dot{\eta}^2 \, sign(\dot{\eta}) \tag{10}$$

in which F_d, $\dot{\eta}$, and d designate damping force, stroke rate, and damping coefficient respectively.

2.3.1. Shock Absorber Coulomb Friction

The calculation of the net Coulomb friction force is presented here following Fled's analysis (Fled, 1990) who computed the equivalent viscous damping contributed by friction in shock absorber bearings and pressure seals. Bearing friction force depends on the normal force acting on it, which is in turn a function of the gear dynamics (Pritchard, 2001). The friction torque resisting the piston's rotational motion is:

$$T_{CLM} = r_p F_t \tag{11}$$

where F_t is the tangential component of the friction force and r_p is the piston radius. The axial component of the friction force F_a resists the axial motion of the piston inside the cylinder. As depicted in Figure 4, the total friction force can be written as:

$$\vec{F} = F_t\vec{e}_\theta + F_a\vec{e}_z \quad (12)$$

$$\left|\vec{F}\right| = \mu N + F_s \quad (13)$$

in which μ and N are the coefficient of friction and time-varying normal force at the bearing respectively. F_s is the force applied by the pressure seal at the bearing location and is assumed to be constant (Fled, 1990). The instantaneous components of the friction force are obtained based on the velocity constituents as:

$$F_t = |F|\frac{-V_t}{\sqrt{{V_t}^2+{V_a}^2}} = (\mu N + F_s)\frac{-r_p\dot{\psi}_l}{\sqrt{r_p^2\dot{\psi}_l^2+\dot{\eta}^2}} \quad (14)$$

$$F_a = |F|\frac{-V_a}{\sqrt{{V_t}^2+{V_a}^2}} = (\mu N + F_s)\frac{-\dot{\eta}}{\sqrt{r_p^2\dot{\psi}_l^2+\dot{\eta}^2}} \quad (15)$$

where V_t and V_a are the tangential and axial components of velocity. The total velocity of a point on the piston (lower strut) relative to the cylinder (upper strut) is then given by $\vec{V} = V_t\vec{e}_\theta + V_a\vec{e}_z$ as depicted in Figure 4. The axial motion is simply captured by the NLG axial DoF (η), hence $V_a = \dot{\eta}$. The tangential displacement is given by $r_p\psi_l$ where ψ_l is the lower strut rotation, therefore $V_t = r_p\dot{\psi}_l$ describes the tangential velocity. The Coulomb torque is then given by:

$$T_{CLM} = r_p(\mu N + F_s)\frac{-r_p\dot{\psi}_l}{\sqrt{r_p^2\dot{\psi}_l^2+\dot{\eta}^2}} = r_p(\mu N + F_s)\frac{-1}{\sqrt{1+(\frac{\dot{\eta}}{r_p\dot{\psi}_l})^2}} \quad (16)$$

As the $\dot{\eta}/r_p\dot{\psi}_l$ ratio grows, the Coulomb torque decreases. Thus, the Coulomb torque reaches its maximum magnitude when the shock absorber is locked axially. However, this is not the scenario in actual ground operations, in which the stroke varies with time.

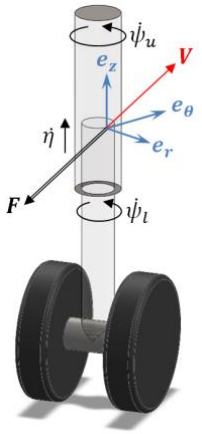

Figure 4. Schematics of shock absorber cylinder- piston motion and their relative velocity

2.3.2. The Influence of Shock Absorber Stroke Rate

One can presume a simple sinusoidal shimmy behavior to take an in-depth look at the effect of piston closure rate on the Coulomb torque. For such a case, the following describes the rotational oscillations:

$$\psi_l = \Psi\, sin(\omega t) \quad (17)$$

$$\dot{\psi}_l = \omega\Psi\, cos(\omega t) \quad (18)$$

Assuming a fixed normal force N, the Coulomb torque may be expressed as:

$$T_{CLM} = r_p(\mu N + F_s)\frac{-r_p\omega\Psi\cos(\omega t)}{\sqrt{r_p^2\omega^2\Psi^2\cos^2(\omega t)+\dot{\eta}^2}} = T_{CLM_{max}}\frac{-\cos(\omega t)}{\sqrt{\cos^2(\omega t)+(\frac{\dot{\eta}}{r_p\omega\Psi})^2}} \qquad (19)$$

The normalized Coulomb torque is plotted for various values of $\sigma = \dot{\eta}/r_p\omega\Psi$ in Figure 5. It is evident that for $\sigma = 0$ the torque is a square wave, while it approaches a straight line as σ grows. The conventional modeling of Coulomb torque as $T_{CLM} = T_{CLM_{max}}\,\text{sign}(\dot{\psi})$ is then only representative for the case of no axial motion.

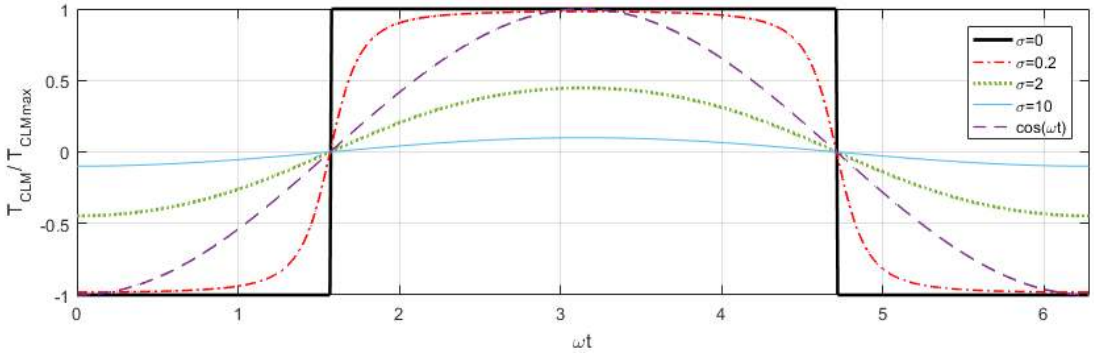

Figure 5. Shock absorber Coulomb torque as a function of $\sigma = \dot{\eta}/r_p\omega\Psi$

3. Multi-Body Dynamic (MBD) Implementation

The dynamic model described in the previous section is implemented in Matlab's SimScape MBD environment for numerical solution. Figure 6 shows the model in the SimScape's Model Explorer, along with the schematic of the MBD model constituents.

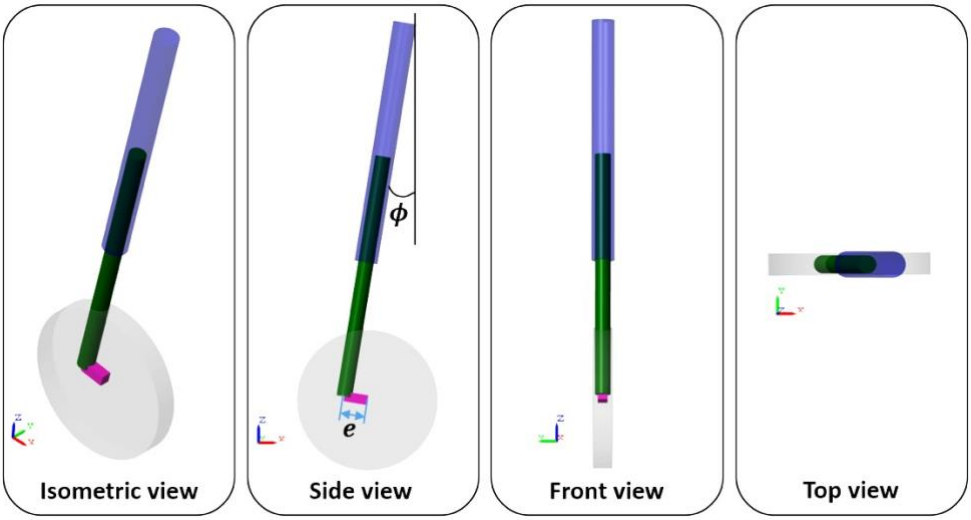

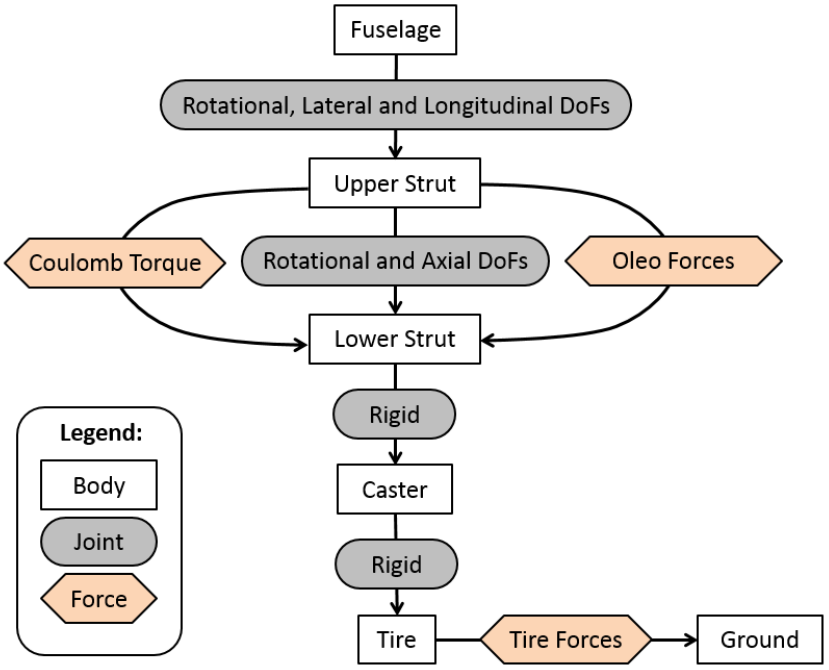

Figure 6. MBD model of NLG in SimScape's Model Explorer in various views (top) and schematic of the MBD constituents (bottom)

The numeric values used by Thota et al. (2008, 2010) are the source for structural, geometry, and tire parameters while shock absorber and Coulomb friction parameters are based on the curves and data presented by Khapane (2003) and Fled (1990) but tuned to accommodate the mid-size NLG data set of Thota et al. (2008, 2010). Table 1 lists all baseline model parameters utilized.

Table 1. Parameter definition and values used in the NLG model

Parameter	Description	Value	Unit
Inputs			
V	Forward velocity	-	ms^{-1}
F_z	Vertical force	-	N
Responses			
ψ	Total rotation of strut end about strut axis	-	rad
δ	Total rotation of strut end about roll axis	-	rad
β	Total rotation of strut end about pitch axis	-	rad
η	Total displacement of shock absorber piston along strut axis	-	m
λ	Tire lateral deflection	-	m
δ^*	Total lateral stroke	-	m
β^*	Total longitudinal stroke	-	m
Structure			
l_{g_0}	Gear height from fuselage attachment to the ground in neutral state	2.5	m
ϕ	Rake angle	0.1571	rad
e	Caster length	0.12	m
I_z	Strut moment of inertia about strut axis	100.0	kgm^2
I_x	Strut moment of inertia about roll axis	600.0	kgm^2
I_y	Strut moment of inertia about pitch axis	750.0	kgm^2
k_ψ	Torsional stiffness of strut	3.8×10^5	$Nm\text{rad}^{-1}$

k_δ	Lateral stiffness of strut	6.1×10^6	$Nm\text{rad}^{-1}$
k_β	Longitudinal stiffness of strut	5.5×10^6	$Nm\text{rad}^{-1}$
c_ψ	Torsional damping of strut	300.0	$Nms\text{rad}^{-1}$
c_δ	Lateral damping of strut	300.0	$Nms\text{rad}^{-1}$
c_β	Longitudinal damping of strut	300.0	$Nms\text{rad}^{-1}$
Tire			
R	Radius of wheel	0.362	m
L	Tire relaxation length	0.3	m
h	Length of tire contact patch	0.1	m
k_α	Self-aligning coefficient of elastic tire	1.0	$m\text{rad}^{-1}$
α_m	Slip angle limit	0.1745	rad
k_λ	Restoration coefficient of elastic tire	0.002	rad^{-1}
c_λ	Damping coefficient of elastic tire	570.0	$Nm^2\text{rad}^{-1}$
Shock Absorber			
F_0	Pre-stress force	1000	N
η_m	Maximum stroke (gas length)	0.6	m
n	Polytropic coefficient	1.18	-
c_k	Correction factor for polytropic coefficient	1	-
d	Oleo square damping coefficient	7.5×10^5	Ns^2m^{-2}
r_p	Piston radius	0.07	m
F_s	Oleo pressure seal force	5000	N
μ	Oleo bearing dry friction coefficient	0.08	-

To verify the model with existing numerical results in literature, a reduced version of the MBD model equivalent to the analytical model presented by Thota et al. (2008) is analyzed first. This version is a fifth-order model with only rotational and lateral DoFs in which all parameters match that of the reference source. As presented in Figure 7, there is a very tight match between the two sets of results for amplitude of lateral and rotational shimmy versus forward velocity.

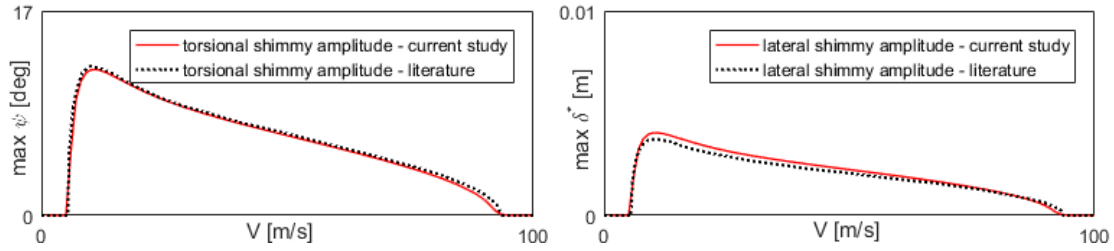

Figure 7. Predicted shimmy amplitudes using MBD model versus results from Thota et al. (2008)

4. Numerical Simulation Results and Discussion

The MBD model constructed in SimScape is numerically solved using built-in Matlab solver $ode23tb$. System inputs are applied in the form of step functions and the dynamics is simulated for 30 seconds. The amplitude plots and shimmy maps are constructed based on the steady-state response with $\psi_{(t=0)} = 0.02$ rad $\approx 1°$ as the initial condition. A linear stability analysis based on eigenvalue calculation is presented at the beginning, which highlights the shimmy trends and key parameter influences.

Case 1: Linear analysis

The equations of motion of the fifth-order NLG model are linearized as follows to perform the linear analyses:

$$I_z\ddot{\psi} + k_\psi\psi + c_\psi\dot{\psi} + M_{T_\psi} + M_{Z_\psi} = 0 \tag{20}$$

$$I_x\ddot{\delta} + k_\delta\delta + c_\delta\dot{\delta} + M_{T_\delta} + M_{Z_\delta} = 0 \tag{21}$$

$$\dot{\lambda} + \frac{V}{L}\lambda - V\psi\cos(\phi) - l_g\dot{\delta} - \left(e_{eff} - h\right)\dot{\psi}\cos(\phi) = 0 \tag{22}$$

where the terms are given as:

$$M_{T_\psi} = \left(k_\alpha F_z\frac{\lambda}{L} + e_{eff}(7k_\lambda F_z\frac{\lambda}{L}) + \frac{c_\lambda}{V}\dot{\psi}\right)\cos\phi \tag{23}$$

$$M_{Z_\psi} = -F_z e_{eff}\psi\cos\phi\sin\phi \tag{24}$$

$$M_{T_\delta} = \left(k_\alpha F_z\frac{\lambda}{L} + e_{eff}(7k_\lambda F_z\frac{\lambda}{L}) + \frac{c_\lambda}{V}\dot{\psi}\right)\sin\phi + l_g F_{k_\lambda}\cos\phi \tag{25}$$

$$M_{Z_\delta} = -F_z e_{eff}\psi\cos^2\phi \tag{26}$$

The state-space representation of the linear system reads:

$$\begin{bmatrix}\dot{\psi}\\ \ddot{\psi}\\ \dot{\delta}\\ \ddot{\delta}\\ \dot{\lambda}\end{bmatrix} = \begin{bmatrix} 0 & 1 & 0 & 0 & 0 \\ \frac{-k_\psi + F_z e_{eff}\cos\phi\sin\phi}{I_z} & \frac{-c_\psi - (c_\lambda/V)\cos\phi}{I_z} & 0 & 0 & \frac{-F_z\left(k_\alpha + 7e_{eff}k_\lambda\right)\cos\phi}{I_z L} \\ 0 & 0 & 0 & 1 & 0 \\ \frac{F_z e_{eff}\cos^2\phi}{I_x} & \frac{-c_\lambda\sin\phi}{I_x V} & \frac{-k_\delta}{I_x} & \frac{-c_\delta}{I_x} & \frac{-F_z\left(k_\alpha\sin\phi + 7k_\lambda(\sin\phi + l_g\cos\phi)\right)}{I_x L} \\ V\cos\phi & \left(e_{eff} - h\right)\cos\phi & 0 & l_g & \frac{-V}{L} \end{bmatrix}\begin{bmatrix}\psi\\ \dot{\psi}\\ \delta\\ \dot{\delta}\\ \lambda\end{bmatrix} \tag{27}$$

Figure 8 presents the stability boundary for baseline system parameters (corresponding to Table 1). For each forward velocity value, a big enough vertical force, designated here as Critical Vertical Force can lead to shimmy. Towards the end of the landing (as speed reduces), a bigger vertical force is experienced by the gear as a result of near-zero lift force from the wings while the Critical Vertical Force is also reduced. Therefore, shimmy is likely to be observed at that situation. Figure 9 shows the sensitivity of the stability boundary as the rotational stiffness and damping are altered. Reducing either of these two properties will shrink the stable zone. Changing the rotational stiffness mostly affects the low-speed region while altering the rotational damping causes a vertical shift in the stability boundary, with a more pronounced effect in the high-speed region. This is significant since shimmy dampers are designed to boost the rotational damping and stiffness of the gear, and the presented trends are valuable in the design of next generation shimmy dampers. Lateral stiffness and damping were found to have no significant influence on the stability boundaries.

Rake angle and caster are typically incorporated in the NLG design to improve the gear stability. The stability boundaries shown in Figure 10 showcases the gains from these features. Increasing the rake angle raises the Critical Vertical Force almost uniformly for most of the forward velocity range. Caster length features a more dominant effect in changing the stable region size, with the effect being more noticeable for higher forward velocities.

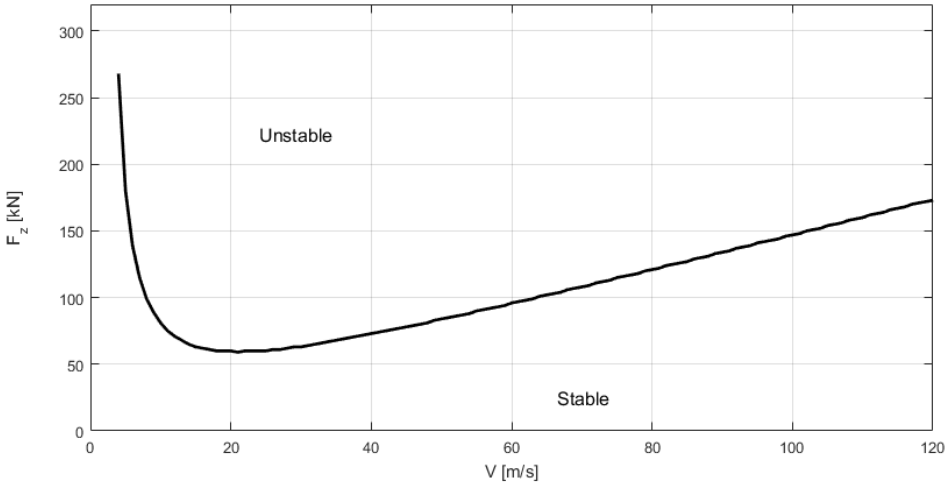

Figure 8. Stability map based on linear analysis of the fifth-order model

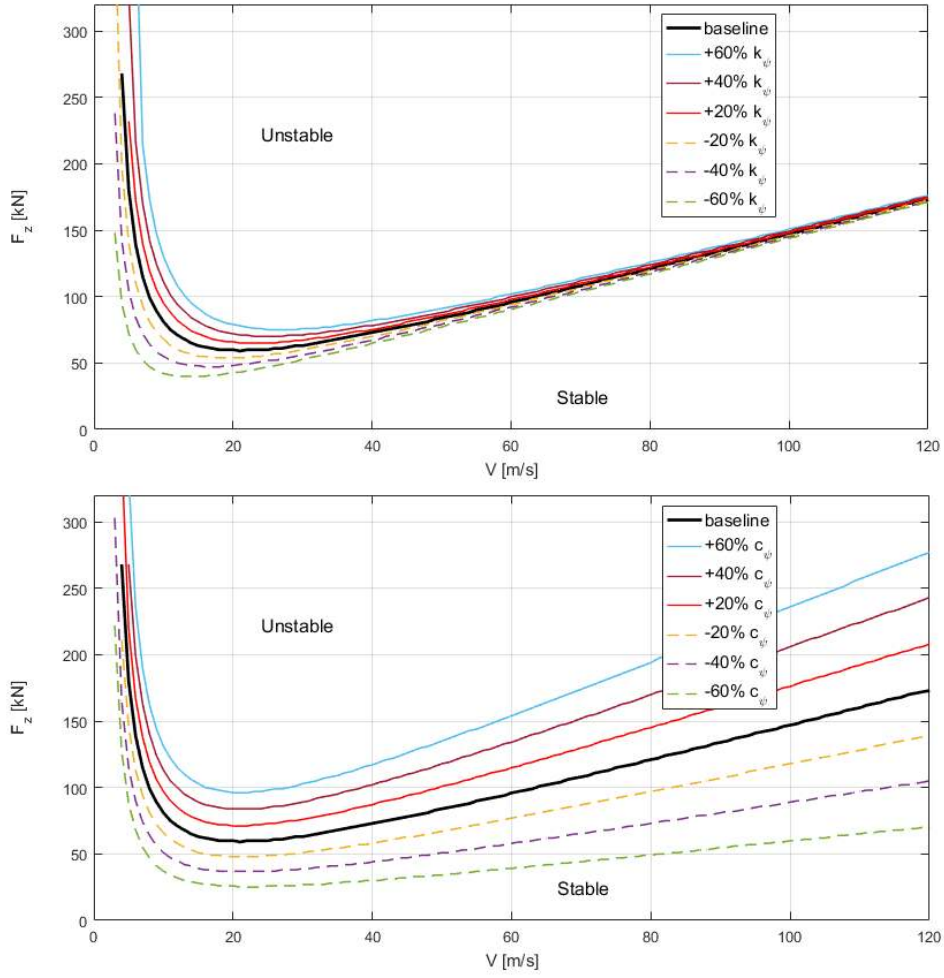

Figure 9. Sensitivity of stability boundary with respect to rotational stiffness k_ψ (top) and rotational damping c_ψ (bottom)

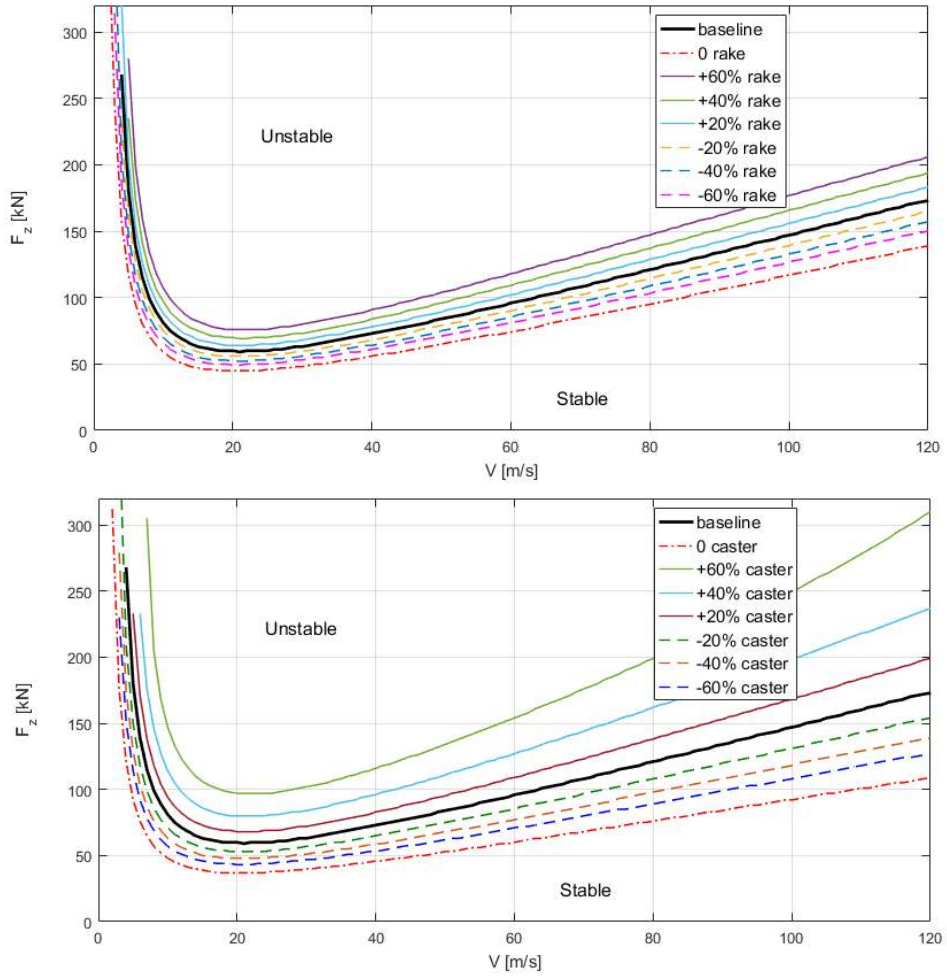

Figure 10. Sensitivity of stability boundary with respect to rake angle ϕ (top) and caster length e (bottom)

Case 2: Fifth-order nonlinear model

The fifth-order MBD model follows the description of the Fundamentals section, except it excludes the longitudinal and axial DoFs. The nonlinearity of this model rises from two sources: the tire's nonlinear force and moment terms, and the moment terms created by the vertical force (M_{Z_ψ}, M_{Z_δ}). The former is the characteristic of the tire model used and the latter is due to the fact that the moment arms involve trigonometric functions of the strut rotational and lateral angles. Figure 11 showcases amplitude plots obtained using this model. The dark blue area common between both rotational and lateral maps designates the stable (no-shimmy) region corresponding to practically zero vibration amplitudes. In the rest of the parameter space both types of shimmy exist; however, only one of the types is dominant. The rotational-dominant region is well signified in the middle of the parameter space, encapsulating large rotational and small lateral amplitudes. The lateral-dominant shimmy region is extended towards high-forward-velocity and high-vertical-force side of the map and is characterized by large lateral shimmy amplitude.

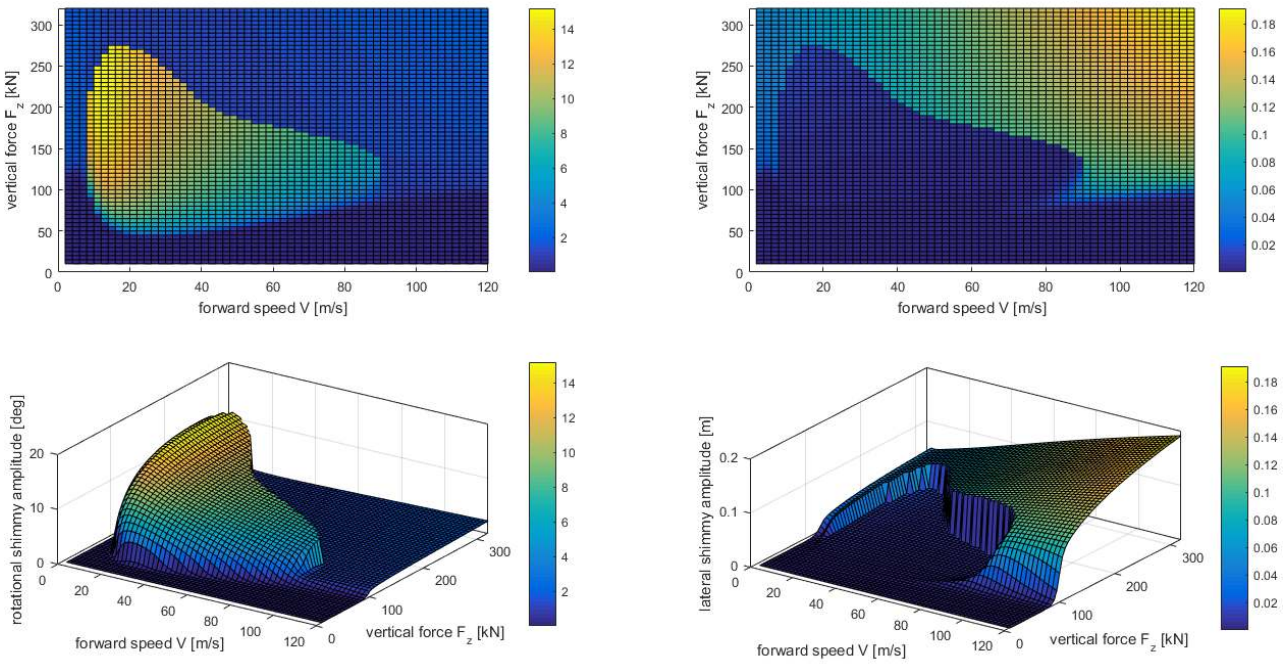

Figure 11. Amplitude plot of rotational (top-left: top view, bottom-left: 3D) and lateral (top-right: top view, bottom-right: 3D) shimmy vibrations for fifth-order nonlinear model

Although similar 3D amplitude plots may be generated for all case studies, comparisons are better achieved using 2D contour maps designating the boundaries of stable, rotational-dominant, and lateral-dominant regions. Figure 12-top features such stability boundaries for Case 2, in which two contour lines are depicted to designate the stable (no-shimmy) and rotational-dominant shimmy regions.

Comparing results of the linear model with Case 2, once realizes that the linear model over-predicts the stable region, while the overall shape of the boundary resembles the no-shimmy line of Case 2. More importantly, the nonlinear model has the advantage of distinguishing between the two types of shimmy. This is key from a design perspective, since it enables design engineers to take preventive measures tailored towards the specific type of oscillations anticipated.

Three points from the parameter space (marked on Figure 12-top) are chosen to showcase example oscillation time histories. These points are located in characteristically different regions of the parameter space, featuring oscillations responses that are qualitatively distinct. As presented in Figure 12-bottom, for point A in the stable region, the oscillations in both DoFs attenuate rapidly and shimmy does not develop. Points B and C are both located in the unstable region, for which stable limit-cycle oscillations are predicted to develop. However, they exemplify the two different shimmy regimes, in which rotational (for Point B) or lateral (for Point C) type of shimmy is dominant.

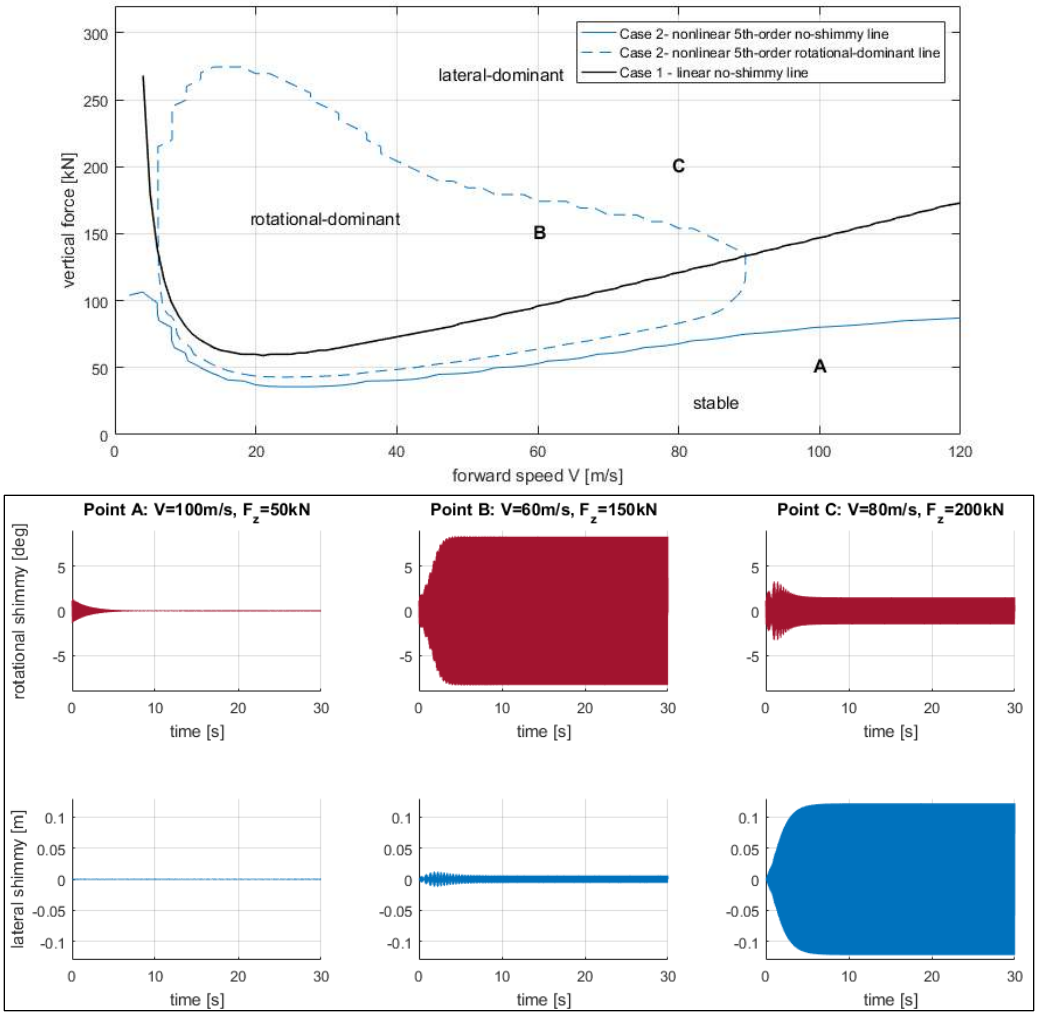

Figure 12. Shimmy boundaries for linear and Case 2 models (top) and time histories of Case 2 oscillations for three different input sets (bottom)

Case 3: Ninth-order nonlinear model

The addition of longitudinal and axial DoFs (including the shock absorber sub-model) to the Case 2 model leads to a ninth-order model with all four DoFs. The nonlinearity of this model stems from nonlinear spring and damper relationships of the shock absorber, in addition to nonlinearity sources of Case 2. In the present case, the LG length varies due to the shock absorber compression and tire vertical compliance. As depicted in Figure 13-top, the no-shimmy line is same as that of Case 2 except for very low and very high speeds, whereas the rotational-dominant region has considerably expanded in Case 3. That is, while addition of axial and longitudinal DoF have not influenced the onset of shimmy in a substantial way, the type of shimmy observed in the unstable region is affected.

Time histories for three parameter instances (marked on Figure 13-top) are shown in Figure 13-bottom. After some time has elapsed, the longitudinal oscillations vanish in all three cases, suggesting that longitudinal stiffness and damping values assumed are high

enough to prevent emergence of Gear Walk oscillations. The axial displacement plateaus after a few seconds due to having a fixed vertical force. However, the contribution of the axial dynamics to the rotational-lateral response may be acknowledged, noting that due to the shock absorber compression the effective gear length decreases, the strut moment of inertia changes, and moment terms based on the vertical force vary.

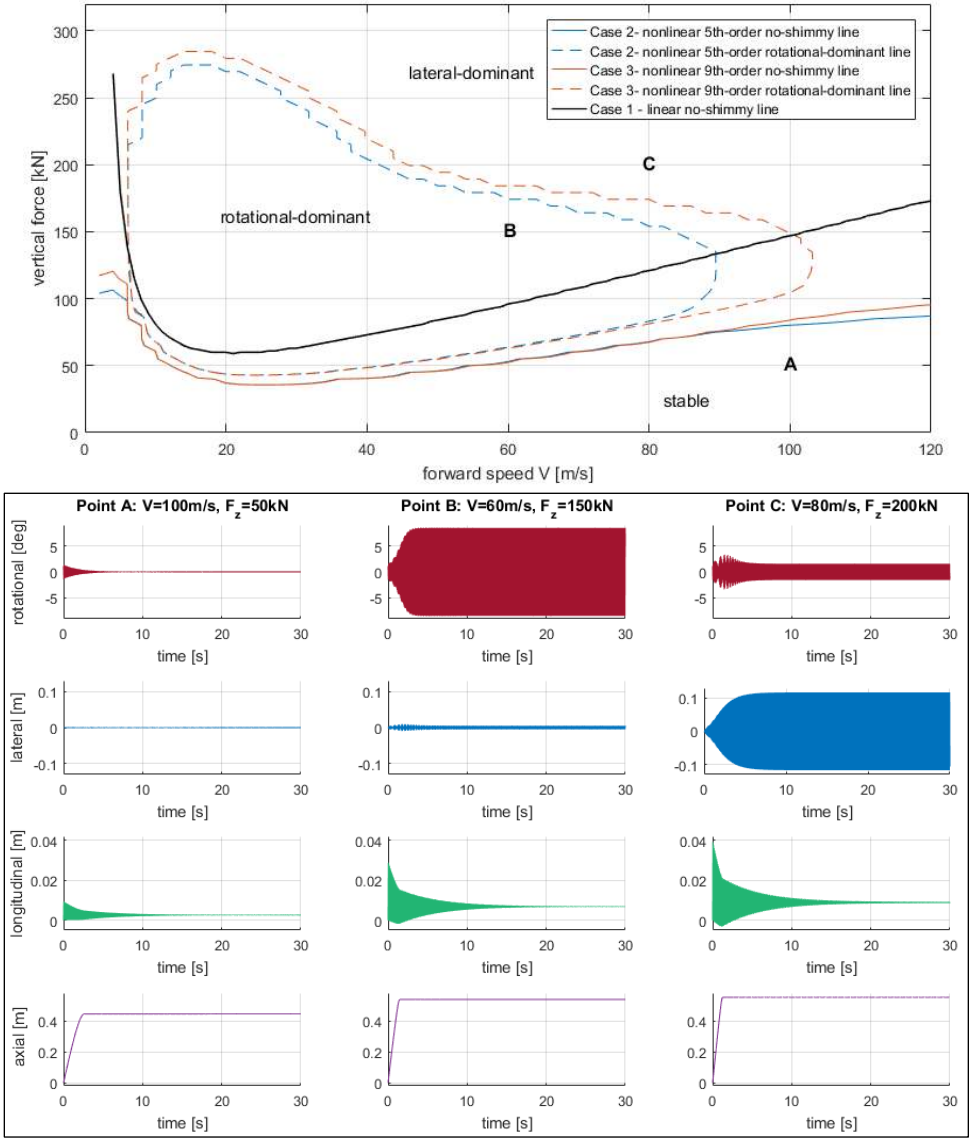

Figure 13. Shimmy boundaries for linear, Case 2 and Case 3 models (top), and time histories of Case 3 oscillations for three different input sets (bottom)

Case 4: Ninth-order nonlinear model with Coulomb torque

In Case 4 model, Coulomb torque is added to the nonlinear ninth-order model of Case 3. This addition is done through a separate module in the MBD model which applies equal amount of torque in opposite directions to the upper and lower struts. The magnitude of the torque is a function of the system dynamics, as per the relationships presented in the Fundamentals section. At all times, the torque is applied in a direction which opposes the

relative rotational motion between the strut pieces. Figure 14-top shows the shimmy boundaries for this model based on the friction parameters assumed in Table 1. Compared to the no-friction case (Case 3) the stable region is expanded, especially for moderate range of speeds. Moreover, the rotational-dominant region is significantly shrunk. This is understood to be due to the resistance from the Coulomb torque which tends to hinder rotational oscillations. Time histories of oscillations for three points (marked on Figure 14-top) are displayed in Figure 14-middle. The histories of Case 4 feature the same shape and trends as Case 3, which is anticipated since the points remain in the same shimmy regimes as in Case 3. However, there are slight changes to the severity of the oscillations observed in Figure 14-bottom, which zooms into the first 4 seconds of rotational oscillations only. For point A in the stable region, Coulomb torque causes the vibrations to vanish more rapidly. Point B in the rotational-dominant shimmy region features stable shimmy limit-cycles as before, but the amplitude of the oscillation has reduced as a result of the energy dissipated through friction. The effect of Coulomb friction on the oscillation of point C is more subtle, which is understood to be due to being located in the lateral-dominant region.

Nonlinear sensitivity studies on the friction parameters are also performed in this section and the collective results are shown in Figure 15. The sub-cases explored are:

Case 4a: No pressure seal force: $F_s = 0$ N, $\mu = 0.08$, $r_p = 0.070$ m

Case 4b: Half friction coefficient: $F_s = 5000$ N, $\mu = 0.04$, $r_p = 0.070$ m

Case 4c: Half piston radius: $F_s = 5000$ N, $\mu = 0.08$, $r_p = 0.035$ m

According to Figure 15, friction coefficient is predicted to have minimal effect on the extent of the stable region while this boundary is shifted by removing the pressure seal force and halving the piston radius. The rotational-dominant shimmy boundary features a qualitatively similar effect, in that halving the friction coefficient has a marginal effect in expanding the rotational-dominant region. Reducing the piston radius appears to have a more significant impact on the rotational-dominant boundary while ignoring the pressure seal force features a stronger effect. These observations are relevant for the specific parameter values used in the case studies and qualitatively different trends may be predicted for a different set of values. Nevertheless, these case studies reveal the importance of detailed modeling of the Coulomb effect in NLG dynamics, from which one can draw design recommendations. For instance, a bigger piston radius is favorable with respect to stability, assuming other design constraints pertaining to the shock absorber are satisfied. One also needs to be aware of the calibration of pressure seals and the choice of piston material and its surface finish. Effects of such choices on the stability needs to be carefully examined by the design team to guarantee the required stability performance for the full range of operation. The nonlinear sensitivity studies are then inevitable to estimate the onset and extent of vibrations and to devise effective shimmy suppression strategies.

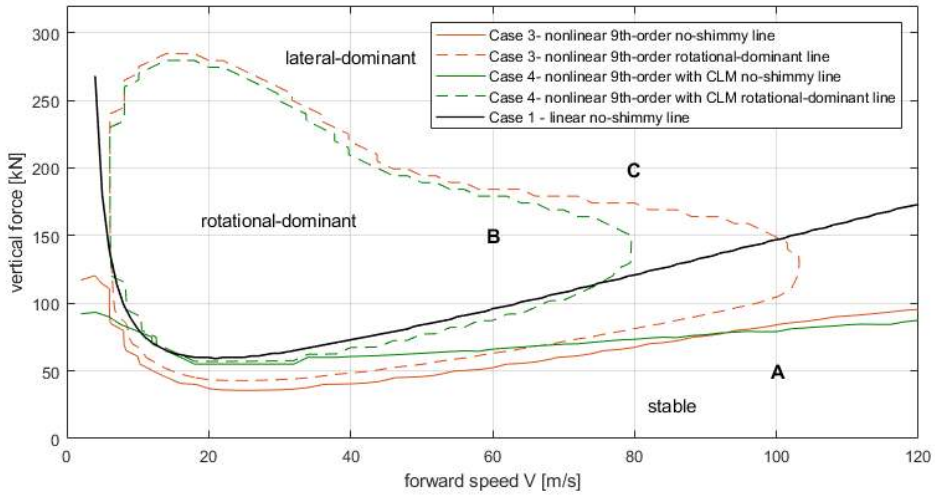
Case 3- nonlinear 9th-order no-shimmy line
Case 3- nonlinear 9th-order rotational-dominant line
Case 4- nonlinear 9th-order with CLM no-shimmy line
Case 4- nonlinear 9th-order with CLM rotational-dominant line
Case 1 - linear no-shimmy line
lateral-dominant
rotational-dominant
stable
A
B
C
vertical force [kN]
forward speed V [m/s]

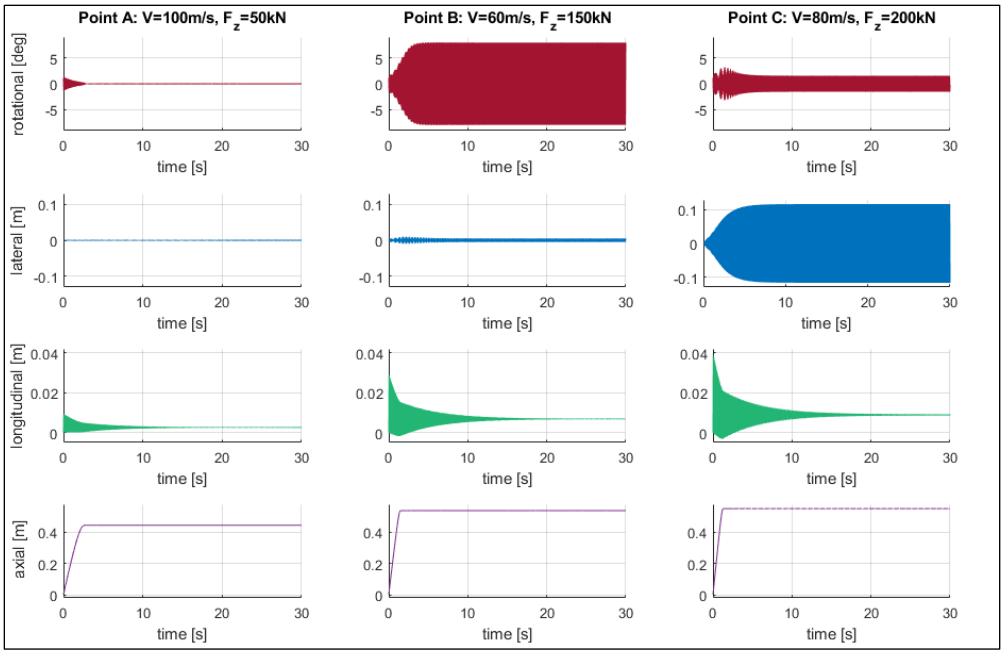
Point A: V=100m/s, F_z=50kN
Point B: V=60m/s, F_z=150kN
Point C: V=80m/s, F_z=200kN
rotational [deg]
lateral [m]
longitudinal [m]
axial [m]
time [s]

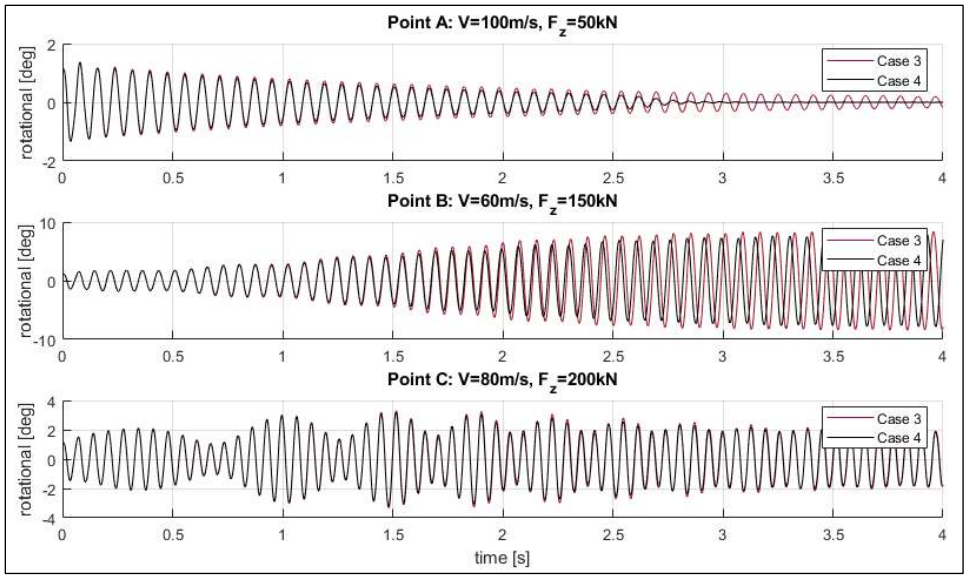
Point A: V=100m/s, F_z=50kN
Point B: V=60m/s, F_z=150kN
Point C: V=80m/s, F_z=200kN
Case 3
Case 4
rotational [deg]
time [s]

Figure 14. Shimmy boundaries for linear, Case 3 and Case 4 models (top), time histories of Case 4 oscillations for three different input sets (middle), and comparison of rotational shimmy amplitudes of Case 3 and Case 4 (bottom)

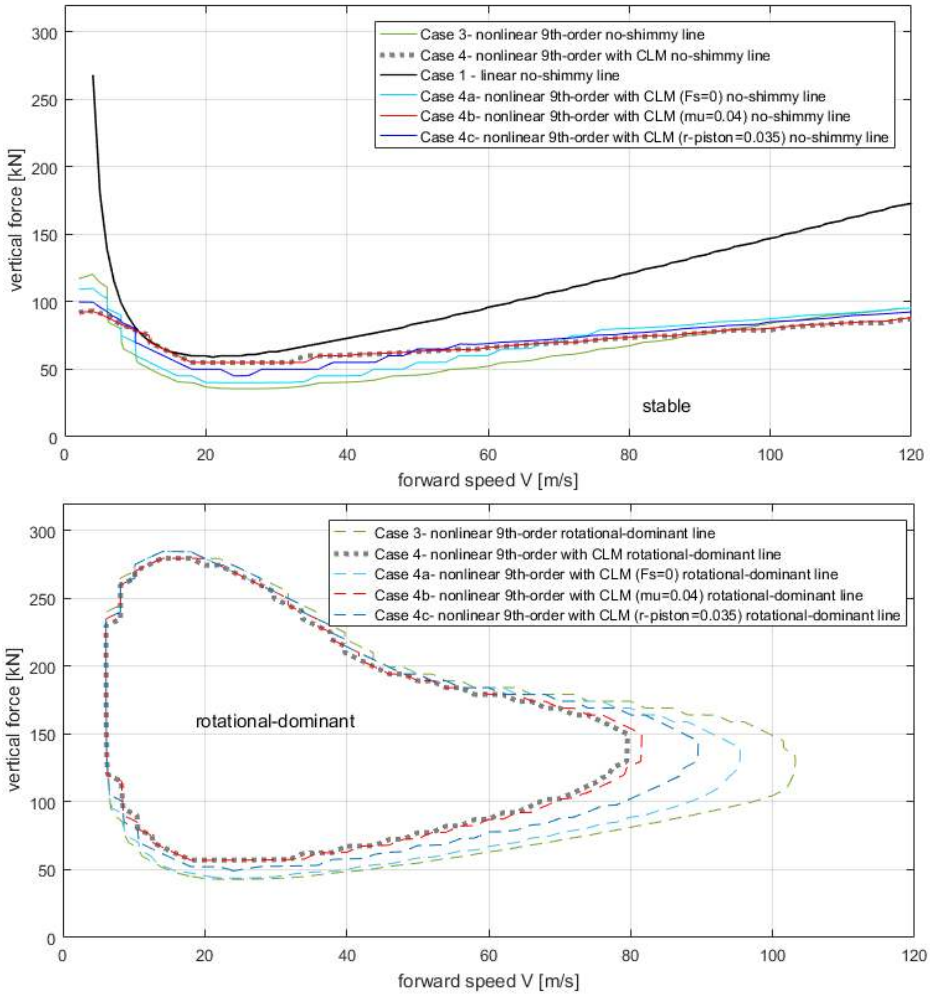

Figure 15. Stable regions (top) and rotational-dominant shimmy regions (bottom) for three sub-cases with different Coulomb parameter sets

5. Conclusion

A detailed MBD model of the NLG system inclusive of all relevant DoFs and significant nonlinearities is presented in this work. The LG industry can benefit from the proposed framework to ensure a shimmy-free design or to minimize the unstable range for new concept designs. The superiority of shimmy maps produced with this approach over conventional stability charts based on linear and quasi-linear analyses is in that first, any nonlinearity can be dealt with using the numerical integration solution and second, using the 3D amplitude maps one has direct access to the severity of the oscillations in addition to the stability boundaries. The importance of the latter is that in practice, oscillations below a threshold might be tolerable and be suppressed with a shimmy damper. To consider this, one cannot merely rely on the stability boundaries and needs to consult the

oscillation amplitudes data. The major contribution of the present work is then proposing an innovative scheme to generate nonlinear 3D shimmy maps and 2D stability charts based on a fully nonlinear NLG model equipped with a novel Coulomb friction sub-model. These maps offer a wealth of information on the gear stability characteristics. Another key contribution is to model the shock absorber Coulomb friction in considerably more detail than the standard approach. The inclusion of this sub-model based on time-varying normal force and shock absorber stroke rate in the fully nonlinear MBD model is a novel work which allows a closer look at the influence of this hard nonlinearity. A particularly innovative aspect of the present study is identifying the effect of Coulomb torque parameters on the gear stability. The nonlinear sensitivity plots highlight the role of each friction parameter, which can be expanded to a more comprehensive Design of Experiment (DoE) study addressing the interactive impact of the parameters. Accounting for the tire vertical flexibility, time-varying length of the gear and using it in calculation of forces and moments, along with the change of structural properties as a function of the shock absorber compression are also important contributions which allow for more accurate and reliable prediction of shimmy oscillations in early stages of the NLG design.
The ongoing extension of this work includes utilizing the MBD model for transient analysis of NLG ground operations which will reveal valuable information on the onset and severity of shimmy oscillations in practical circumstances. Data from ground operation tests needs to be used as time-varying inputs in such simulations. Ultimately, this work will close the gap between numerical simulation and physical testing of shimmy phenomena in NLGs by providing realistic predictions and permitting thorough investigation of design parameters. The envisioned framework whose fundamental methods and analyses are unfolded in this paper delivers a comprehensive view of the NLG stability characteristics and offers strategies for shimmy-free NLG design.

Funding

The authors gratefully acknowledge the research grant provided by Sumitomo Precision Products Canada Aircraft Inc. (SPPCA) and Natural Sciences and Engineering Research Council of Canada (NSERC) in support of this work.

References

Arreaza C, Behdinan K and Zu J (2016) Linear stability analysis and dynamic response of shimmy dampers for main landing gears. *Journal of Applied Mechanics* 83(8): 081002-081002-10.

Atabay E and Ozkol I (2013) Application of a magnetorheological damper modeled using the current–dependent Bouc–Wen model for shimmy suppression in a torsional nose landing gear with and without freeplay. *Journal of Vibration and Control* 20(11): 1622-1644.

Burton TD (1981) Describing function analysis of nonlinear nose gear shimmy. ASME Paper 81-WA/DSC-20.

CIAIAC (1999) Accident of aircraft Fokker MK-100, registration I-ALPL, at Barcelona Airport (Barcelona), on 7 November 1999. Technical Report A-068/1999.

Coetzee E (2007) *Shimmy in aircraft landing gear*. Airbus Study Group report.

Daniels JN (1996) *A method for landing gear modeling and simulation with experimental validation*. NASA Contractor Report 201601.

Eret P, Kennedy J and Bennett G (2015) Effect of noise reducing components on nose landing gear stability for a mid-size aircraft coupled with vortex shedding and freeplay. *Journal of Sound and Vibration* 354: 91-103.

Esmailzadeh E and Farzaneh K (1999) Shimmy vibration analysis of aircraft landing gears. *Journal of Vibration and Control* 5(1): 45-56.

Feng F, Nie H, Zhang M and Peng Y (2015) Effect of torsional damping on aircraft nose landing-gear shimmy. *Journal of Aircraft* 52(2): 561-568.

Fled DJ (1990) An analytical investigation of damping of landing gear shimmy. *SAE Technical Paper* 902015.

Gordon J (2002) Perturbation analysis of nonlinear wheel shimmy. *Journal of Aircraft* 39(2): 305-317.

Grossman DT (1980) F-15 nose landing gear shimmy, taxi test and correlative analyses. *SAE Technical Paper* 801239.

Gualdi S, Morandini M and Ghiringhelli G (2008) Anti-skid induced aircraft landing gear instability. *Aerospace Science and Technology* 12(8): 627-637.

Howcroft C, Lowenberg M, Neild S and Krauskopf B (2013) Effects of freeplay on dynamic stability of an aircraft main landing gear. *Journal of Aircraft* 50(6): 1908-1922.

Howcroft C, Lowenberg M, Neild S, Krauskopf B and Coetzee E (2015) Shimmy of an aircraft main landing gear with geometric coupling and mechanical freeplay. *Journal of Computational and Nonlinear Dynamics* 10(5): 051011-051011-14.

Kewley S, Lowenberg M, Neild S and Krauskopf B (2016) Investigation into the interaction of nose landing gear and fuselage dynamics. *Journal of Aircraft* 53(4): 881-891.

Khapane P (2003) Simulation of asymmetric landing and typical ground maneuvers for large transport aircraft. *Aerospace Science and Technology* 7(8): 611-619.

Khapane P (2006) Gear walk instability studies using flexible multibody dynamics simulation methods in SIMPACK. *Aerospace Science and Technology* 10(1): 19-25.

Krason W and Malachowski J (2015) Multibody rigid models and 3D FE models in numerical analysis of transport aircraft main landing gear. *Bulletin of the Polish Academy of Sciences Technical Sciences* 63(3):

Krüger W and Morandini M (2011) Recent developments at the numerical simulation of landing gear dynamics. *CEAS Aeronautical Journal* 1(1-4): 55-68.

Krüger W, Besselink I and Cowling D et al. (1997) Aircraft landing gear dynamics: simulation and control. *Vehicle System Dynamics* 28(2-3): 119-158.

Liu Y, Chen M and Tian Y(2015) Nonlinearities in landing gear model incorporating inerter. In: *IEEE International Conference on Information and Automation*, Lijiang, China.

Lok S, Paul J and Upendranath V (2014) Prescience life of landing gear using multiaxial fatigue numerical analysis. *Procedia Engineering* (86): 775-779.

Moreland W (1954) The story of shimmy. *Journal of the Aeronautical Sciences* 21(12): 793-808.

Pacejka H (2009) *Tyre and vehicle dynamics*. Amsterdam: Elsevier Butterworth-Heinemann.

Padmanabhan M and Dowell E (2015) Landing gear design/maintenance analysis for nonlinear shimmy. *Journal of Aircraft* 52(5): 1707-1710.

Pritchard J (2001) Overview of landing gear dynamics. *Journal of Aircraft* 38(1): 130-137.

Somieski G (1997) Shimmy analysis of a simple aircraft nose landing gear model using different mathematical methods. *Aerospace Science and Technology* 1(8): 545-555.

Somieski G (2001) An eigenvalue method for calculation of stability and limit cycles in nonlinear systems. *Nonlinear Dynamics* 26(1): 3-22, 2001.

Sura N and Suryanarayan S (2007) Lateral response of nose-wheel landing gear system to ground-induced excitation. *Journal of Aircraft* 44(6): 1998-2005.

Thota P, Krauskopf B and Lowenberg M (2008) Interaction of torsion and lateral bending in aircraft nose landing gear shimmy. *Nonlinear Dynamics* 57(3): 455-467.

Thota P, Krauskopf B and Lowenberg M (2010) Bifurcation analysis of nose-landing-gear shimmy with lateral and longitudinal bending. *Journal of Aircraft* 47(1): 87-95.

Van Der Valk R and Pacejka H (1993) An analysis of a civil aircraft main gear shimmy failure. *Vehicle System Dynamics* 22(2): 97-121.

Von Schlippe B and Dietrich R (1947) *Shimmying of a pneumatic wheel*. Report submitted to the National Advisory Committee for Aeronautics, NACA TM 1365.

Zegelaar P and Pacejka H (1996) Dynamic tyre responses to brake torque variations. *Vehicle System Dynamics* 27: 65-79.

Zhou J and Zhang L (2005) Incremental harmonic balance method for predicting amplitudes of a multi-d.o.f. non-linear wheel shimmy system with combined Coulomb and quadratic damping. *Journal of Sound and Vibration* 279(1-2): 403-416.